NASA Technical Memorandum 4129

Photogrammetric Technique Using Entrained Balloons for In-Flight Ranging of Trailing Vortices

Walter L. Snow, Alpheus W. Burner,
and William K. Goad

OCTOBER 1989

NASA

NASA Technical Memorandum 4129

Photogrammetric Technique Using Entrained Balloons for In-Flight Ranging of Trailing Vortices

Walter L. Snow, Alpheus W. Burner,
and William K. Goad
Langley Research Center
Hampton, Virginia

National Aeronautics and
Space Administration
Office of Management
Scientific and Technical
Information Division

1989

Introduction

It is well known that wingtip vortices shed by heavy aircraft can prove extremely hazardous to trailing aircraft. (See refs. 1 and 2.) Tip vortices may persist at significant strengths for over 5 miles. The extremely large rolling and yawing moments induced in an aircraft whose flight path is nearly aligned with the vortex core may exceed the ability of the control surfaces to compensate, with possible disastrous consequences. Furthermore, at low altitudes there is little time for the pilot to recover from a flow-induced upset. The longitudinal spacings necessary to assure vortex safety have become a major deterrent to improving airport capacity.

NASA has supported FAA programs to model and study the wingtip vortex problem by measuring pertinent variables in the wake of the generating aircraft. Measurement variables include airspeed, altitude, angle of attack, sideslip angle, accelerations, rotation rates about body axes, etc., which are available as continuous analog records as the instrumented trailing aircraft interacts with the wake. Although smoke is routinely used to enhance the visibility of wingtip vortices, there are no currently accepted schemes to quantitatively measure the location of the vortex relative to the trailing aircraft. In vortex interaction studies, it is the perpendicular distance from the vortex core to the perturbed aircraft (D_c in fig. 1) which is of primary interest. D_c should be measured while the aircraft acquires data pertinent to the verification of the interaction model. The expected range of D_c is 50 to 250 ft.

Since the low-pressure vortex core is known to attract neutral buoyancy tracers in aerodynamic studies, this paper suggests that photogrammetric techniques (using the tracers as targets) might be applicable if several operational difficulties associated with targeting and camera mounting can be surmounted. This paper suggests the use of time-encoded stereo images to correlate with onboard sensor records. Postflight analysis using standard photogrammetric methods would triangulate the positions of suitable targets entrained in the vortex core, and analytic geometry would be used to locate the core with respect to the sensing aircraft based on these measured target positions.

The limited scope of this investigation was not to optimize an implementation of the scheme but rather to uncover any insurmountable weaknesses in the approach, while presenting the essentials to nonspecialists in photogrammetric techniques. It was assumed that the easiest and cheapest viable option would involve equipping a general aviation probe aircraft with fuselage-mounted cameras. Solid-state television cameras were also assumed since they can provide data at needed framing rates (30 Hz), are rugged, and were available for this investigation. The targeting problem is recognized, but only superficially treated here. Practical methods of seeding the core with balloons or other suitable targets at flight altitudes are being pursued as a parallel effort but are not discussed here.

Experimental Approach

Concept

The proposed measurement technique is based on time-tested photogrammetric principles. (See ref. 3.) The basic description requires no mathematics beyond plane geometry and is modeled by projective transformation. In figure 2 a point $P(X, Y, Z)$ in three-dimensional space projects through perspective center O onto a two-dimensional surface (usually planar) as point $p'(x', y')$. The mapping has no unique inverse because knowledge of p' and the perspective center alone defines points along the entire ray containing O and p'. The ranging ambiguity is removed, however, if a second station is added as in figure 3. For ease in visualizing the pertinent similar triangles, the geometry is exaggerated and the *cameras* are oriented with parallel axes separated by baseline B. In practice the camera axes converge to improve scene overlap. From similar triangles (solid lines),

$$\frac{Z}{X + (B/2)} = \frac{c}{x'} \tag{1}$$

The triangles outlined with dashed lines give

$$\frac{Z}{X - (B/2)} = \frac{c}{x''} \tag{2}$$

Eliminating X and solving for Z gives

$$Z = \frac{Bc}{(x' - x'')} \tag{3}$$

The range is thus recovered in terms of camera geometry (e.g., B), camera parameters (e.g., c), and measured stereoscopic parallax $p_x \equiv x' - x''$. In practice, camera location (three spatial coordinates) and orientation (rotations about the coordinate axes) are determined by matching a known set of object coordinates with the corresponding measured images in a process known to photogrammetrists as resection. The resection phase also determines the primary coordinate system for subsequent measurements. The resulting collinearity equations provide the cornerstone for photogrammetry and are derived in the appendix. Implicit in the previous derivation is the

assumption that object point, image point, and perspective center lie on a straight line. Practically, this is not true because of geometrical aberrations in the lens. Methods for calibrating lens distortion are well established and are described, for example, in references 4 and 5. The measured image coordinates are preprocessed to remove distortion before their use in the collinearity equations. Further considerations involved with using solid-state array cameras for photogrammetry are described in reference 5.

Geometrical Considerations

To minimize the effects of unavoidable measurement errors in determining object point coordinates, one usually tries to *strengthen* the geometry, to use the jargon of photogrammetry. A *strong* geometry may be thought of as one that maximizes the stereoscopic parallax (e.g., p_x) for the greatest number of points. In equation (3) we have arbitrarily chosen Z as the dependent variable. Since B, c, and p_x may all be determined independently of one another and enter linearly into the relationship, the elementary working rule of measurement applies, namely, that the relative error in measuring a dependent variable is the sum of the relative errors in determining the independent variables. This can be demonstrated mathematically by taking the total differential of equation (3) and associating incremental error with the differentials (e.g., $dZ = \Delta Z$, etc.). In particular,

$$\left|\frac{\Delta Z}{Z}\right| = \left|\frac{\Delta B}{B} + \frac{\Delta c}{c} + \frac{\Delta p_x}{p_x}\right| \leq \left|\frac{\Delta B}{B}\right| + \left|\frac{\Delta c}{c}\right| + \left|\frac{\Delta p_x}{p_x}\right| \qquad (4)$$

In this simplified, parallel axis geometry, the three independent sources of triangulation error involving external geometry, camera characterization, and image measurement are encompassed by B, c, and p_x, respectively. *Limiting error* is a term introduced by Brown (ref. 6) and represents the best case accuracy, which occurs when the first two terms on the right-hand side of equation (4) are negligible, i.e., when exterior and interior orientation are exactly known. The unavoidable random error inherent in measurement of plate coordinates becomes less important as p_x becomes large and is the basis for wanting strong geometry. In practical applications the experiment restricts complete freedom of camera placement. For this work one might conceivably locate the cameras along the fuselage axis of the aircraft.

For reasonable ranging accuracy (e.g., see eq. 16.20 of ref. 3) B is chosen to be greater than or equal to $Z_{\max}/20$, or 12.5 ft for this application. The minimum useful working distance, primarily due to lack of scene overlap, is on the order of $5B$, or 62.5 ft. This baseline separation requirement is consistent with the dimensions of a light aircraft. Figure 4 depicts a typical solid-state camera. With an active sensor area of 8.8 by 6.6 mm and equipped with a 12.5-mm focal length lens, this camera would have a 38° field of view. Two cameras at each of two sites allow more complete coverage. For illustration, a plan view of a four-camera configuration is shown in figure 5. The figure is drawn to scale. With two cameras at each site, the field of view is $2 \times 38°$, or 76°. Targets can be ranged as long as they occur within the hatched overlap area. Range vectors, arbitrarily labeled $\mathbf{R}_1$ and $\mathbf{R}_2$, to balloons are shown in the figure.

Equation (4) serves to crudely estimate limiting accuracy. Note from equation (3) that $p_x = Bc/Z$ and that the useful range is such that $5B < Z < 20B$. Therefore $c/5 > p_x > c/20$. With our pixel dimension (11.5 μm) as a unit of measure, $c =$ 12.5 mm = 1087 pixels, therefore, $217 > p_x$ [pixels] > 54. For fixed camera parameters the ranging accuracy will depend only on relative parallax error and will vary from 0.5 percent at 50 ft to 2 percent at 250 ft, assuming relatively crude 1-pixel centroiding accuracy. The centroid of high-contrast targets can usually be determined five times more accurately than that with consequent improvement in ranging accuracy. Increasing the camera constant to increase the parallax and hence reduce the ranging error also reduces the field of view and induces "tunnel vision," which makes capturing a target in the scene less probable.

If the cameras are placed on the probe aircraft, then the baseline separation would be limited by the overall dimensions of light general aviation aircraft. Baseline B could be scaled up significantly, however, if cameras were mounted on a much larger auxiliary aircraft overflying the experiment, thus providing the perspective shown in figure 5. For example, suppose that the cameras exploited the dimension of a commercial airliner to provide $B = 200$ ft. Then, using the same rule of thumb, the working range would be 1000 to 4000 ft above the action, and the minimum footprint size of the sensor would be roughly 500 by 700 ft (vs. 30 by 40 ft earlier), making it much more probable to have targets in the scene. Obviously, in this scenario, the probe aircraft would also be targeted so that its location relative to the vortex targets could be determined. Maintaining tolerable ranging accuracy would require subpixel centroiding accuracy.

At any epoch, the vortex is describable by some space curve which, locally, to first order, can be described by a straight line. The stated objective of this investigation is to determine the proximity of

the probe aircraft to the vortex core (D_c in fig. 1). In this case, which is depicted in figures 5 and 6, the vortex core lies along line $\mathbf{R}_1 - \mathbf{R}_2$. In this diagram cameras 1 and 2 are located by position vectors $\mathbf{R}_1^c$ and $\mathbf{R}_2^c$ respectively. Recall that these vectors are in a coordinate system determined by the known object points of the reference field used to resect camera positions, and this coordinate system remains fixed with respect to the aircraft thereafter. In this diagram $\mathbf{R}_{\text{avg}}$, which bisects the camera baseline, may be used to characterize the position of the aircraft in space. Let P_1 and P_2 be two points on the line. These could be actual individual targets or arbitrary points on a line determined by least squares fitting of several target triangulations. Then let $\hat{u}_1$ be a unit vector along line segment $\mathbf{R}_1 - \mathbf{R}_2$ and $\hat{u}_2$ be a unit vector along $\mathbf{R}_{\text{avg}} - \mathbf{R}_2$. Then, $\cos(\gamma) = (\hat{u}_1 \cdot \hat{u}_2)$ and the required distance D_c is given by

$$\begin{aligned} D_c &= |\mathbf{R}_{\text{avg}} - \mathbf{R}_2| \sin(\gamma) \\ &= |\mathbf{R}_{\text{avg}} - \mathbf{R}_2| \sqrt{1 - (\hat{u}_1 \cdot \hat{u}_2)^2} \end{aligned} \tag{5}$$

When the vortex core describes a more tortuous curve in space, given a suitable number of entrained targets, photogrammetry is still well suited for defining the path, although "proximity to the core" becomes somewhat tenuous. If only one target appears in the frame, one could use a zeroth-order approximation and use its range as an estimate of D_c. More sophisticated single-target analysis would entail assumptions about the aircraft trajectory, time dependence of the measurement field, etc.

Targets

Implicit in the description of photogrammetric measurements is the requirement for crisp identifiable targets recorded at the same time by both cameras. Corresponding targets must be accurately located on at least two separate images. The absence of chapters on targeting in photogrammetry manuals belies the fact that photogrammetrists take great pains to devise schemes to enhance identifiable marks on the object to be measured so that the targets dominate the background clutter in the image. In some instances active (e.g., light emitting) targets are introduced at considerable expense and effort to solve the problem, especially in cases where near real-time control is desired as an outcome of the experiment.

Since it would be reasonably easy to entrain smoke into the trailing vortex, it was hoped that identifiable wisps might serve as suitable triangulation targets. To this end a video camera was used to view the effluent from a small laboratory smoke generator placed outdoors. Although the eye clearly distinguished large-scale structure, the reliable identification of a small feature on two images required for triangulation was not possible.

Experimental aerodynamicists sometimes use neutrally buoyant bubbles to visually locate vortex cores. The reduced pressure distribution within the core provides for natural containment of the bubbles. In controlled tunnel environments the bubbles are strongly illuminated in darkened surroundings to make them more visible. As an adjunct to the previous experiment, soap bubbles were released outdoors and viewed with the same camera. Though visible, the contrast under ambient conditions was judged sufficiently low to preclude their further use as suitable triangulation targets. Ping-Pong balls sprayed with retro-reflective paint and used in conjunction with flash lamps might be used if their mass (2.4 g) did not preclude them dynamically from residing in the core. While there is unanimous agreement that particles of neutral bouyancy seek the core of a free vortex, the fate of heavier particles usually prompts debate. Simplistic arguments would suggest that centrifugal forces dominate such situations and rapidly expel the particles. Experimental evidence (e.g., see ref. 7) shows that particles of specific gravity 2 in a free vortex in water indeed stabilize at fixed radii and suggests that fluid pressure forces not accounted for in simpler analytical models might be responsible. Flight experimentation with various target and deployment schemes seems warranted to resolve the issue. An ideal target should be neutrally buoyant to seek out the vortex core and should have optical scattering properties which would make it appear distinct against a sky background in sunlight. Interpolation to subpixel accuracy necessarily involves images which cover several pixels. For close-range photogrammetry this can usually be accomplished by increasing target size. Larger targets scatter more light and are visible at longer distances. The image size decreases as the target recedes only to the extent limited by diffraction. The Airy disk diameter in pixels is 0.17 $\times$ the f-number of the lens, assuming 0.8-μm wavelength light and 11.5-μm pixels. So for f-numbers greater than 8, even a star, whose geometric image size approaches zero, spans more than one pixel.

Figures 7 and 8 are included for illustrative purposes. A Mylar party balloon (fig. 7) was photographed with a charge-coupled device (CCD) camera at a distance of about 900 ft. One surface of the balloon is specular and the other is not, as shown in the top of the figure. The balloon was taped to the end of a measuring stick and held at arms length as illustrated in the lower photograph. For the

actual experiment, the holder was on the hangar roof in the background. At that distance (900 ft) the white shirt of the experimenter was barely discernible to the eye and not at all by the camera. Twenty consecutive frames of data were acquired over a 1-sec interval. Figure 8 shows wire mesh plots of the gray levels of pixels in the neighborhood of the target. The tie points of the mesh represent pixel intensity. The balloon gyrated wildly in the wind and the shiny side provided momentary glints which show as elevations above the fairly high and constant sky background. The geometric image of this 20-in. target would scale to a couple of pixels at this distance. In this instance the lens was neutral density filtered and the aperture was at f/2. The data measurement involves calculating the center of mass of these light irradiance solids in the xy plane. Highly reflective Mylar type balloons or retro-reflective balloons accompanied by suitable flash could provide suitable targets for this application if the awkwardness of deploying them could be overcome.

Documentary film prepared by AeroVironment, Inc., for NASA in 1971 in conjunction with flight vortex studies provides excellent verification of the balloon entrainment concept. Several dozen helium-filled balloons were released from the ground. A light general aviation airplane passed over the ascending swarm. As the balloons entered the influence of the wingtip vortices, they "snapped" into position to delineate the core. Enlargements of two frames of the 16-mm film clip are shown as figure 9. In the upper photo the balloons display random position. In a later frame shown below it, they are beginning to line up inside the vortex core. These pictures do not do justice to the visual impact of the film clip. It is as if the balloons are loosely tethered together and suddenly the string is drawn taught. The balloons literally "snap" into position and seem to be fixed on an invisible space curve presumably defined by the vortex core.

A practical implementation of balloon seeding could be awkward. A proper characterization of the core would require a target every 100 ft or so. About 50 balloons per mile of data would be required assuming perfect entrainment with deployment rates of several per second for normal flight speeds. Since some balloons might escape capture, an oversupply would have to be launched to allow for vagrants. A preliminary attempt to entrain balloons launched from a Shorts Skyvan into its own trailing vortices was made in April 1989 at the NASA Wallops Flight Facility. Several hundred helium- and nitrogen-filled balloons were expelled from the rear hatch. The tests were conducted over the runway at 500 and 1000 ft and photographed by ground-based observers. All but about six of the balloons were downwashed and settled to the ground. The few that found themselves close enough to the core were seen to gyrate wildly as they were captured. Release closer to the wingtip is clearly advisable but also more difficult to implement.

Laboratory Tests

An existing (see ref. 5) video-based model deformation system was used to investigate the potential accuracy of the proposed technique. The original system, which is fully described in reference 5, is designed for a 5- to 10-ft working range, which is one to two orders of magnitude less than that for the intended vortex localization application proposed here. One objective of the testing was to assess the effect of scaling to a larger working volume. Another objective was to examine the consequences of having a moving reference frame as opposed to a fixed frame and changing object field as was the case for reference 5.

The original system includes an IBM AT computer which controls two Silicon Video image capture boards ganged to allow simultaneous capture of a pair of 752 (horizontal) $\times$ 480 (vertical) pixel images in 1/30 sec. Software written in C programming language allows the PC to digitize, process, display, and store video images. The video images, which are stored as DOS files, can be randomly read with user-developed code (BASIC or C) for computation of centroids. Cohu Model 4815 frame transfer CCD cameras having nominal pixel dimensions of 11.5 μm (horizontal) $\times$ 27 μm (vertical) with an effective vertical pixel spacing of 13.5 μm due to interlace were used for the tests. Standard 13-mm focal length lenses attenuated with neutral density filters and stopped to f/4 or f/16 were used for imaging. Cameras and lenses were characterized using optical shop techniques, some of which are described in reference 5. A more accurate technique was developed to determine the camera constant c since it is likely that triangulation will occur outside the volume encompassed by the resection set. Partial error compensation can occur within the resection volume by adjustment of other variables in the problem. Lens corrections modeling for distortion and lens decentering (i.e., three parameters) fell slightly short of expectations based on previous work with 25-mm lenses. Residuals after corrections warrant added effort for future enhancements.

Several experiments were conducted on the laboratory roof to provide an opportunity for viewing targets against a natural sky background. A typical testing situation is shown in figure 10. Cameras were mounted 12 ft apart on an aluminum bar which was,

in turn, mounted on a tripod. Part of the tripod and one of the cameras are visible in the lower left of the photo. This arrangement corresponds roughly to a fuselage mount arrangement with the aircraft at a shallow angle to the core. Targets were tied to a 150-ft cable simulating the vortex core. The cable ranged from shoulder height to nearly 20 ft above the roof. Tensioning was insufficient to completely linearize the natural catenary shape of the cable. In the figure, cardboard disks were used instead of balloons. Balloons tethered to the cable tended to gyrate wildly in the mildest of breezes and burst as they chaffed against the cable.

Two independent sets of reference targets are also visible in the photo. Twenty-one planar targets are arrayed on a 4 × 8 ft sheet of plywood in the foreground. A nonplanar set covering a much larger volume (140 × 40 × 7 ft) is arranged on closet rods affixed to weighted wooden stands. Either of these sets of "known" targets can be used to resect the camera locations and orientations. Ideally a set of control points used for resection should encompass the desired measurement volume.

Providing a large set of reference targets is not trivial. In this case, lasers and precision splitter cubes were used to provide an orthogonal grid of poles. Construction tapes and levels were then used to establish the absolute coordinates. The horizontal coordinates of the large reference set had the largest uncertainties because of the variation in the vertical orientation of the somewhat flimsy poles and were estimated to be less than 3 in. The vertical coordinate uncertainty was estimated to be less than 0.5 in. For the large reference set the image plane residuals for the resection were 11 μm in x and 3 μm in y, whereas, for the small reference set (4 × 8 ft sheet of plywood), the residuals were 1 μm in x and 3 μm in y. The increased error noted in the large reference set reflects the difficulty in establishing a large control volume under field conditions and also the large (up to 1/2 pixel) uncorrected distortion at the extremes of the large reference field which covers a much larger span in the sensor's x-direction. Note that neither control set encompasses the desired measurement volume. The experiment depicted in figure 10 involved target pairs separated by 25 to 125 ft, which is considerably less than that expected in flight tests. Balloons launched from the generating aircraft at several per second would be spaced several hundred feet apart at cruising speeds. The compressed scale was dictated by the limited expanse of the roof. For this test the perpendicular distance to the cable (core) was measured with a steel tape and found to be 37.6 ft. Figure 11 summarizes the results for one data sequence. Four image pairs were taken with the baseline fixed in each of two orientations. A partial sketch of the two camera views is shown in figure 11(a) with targets labeled to correspond with figure 10. The circles correspond to the baseline position 1 and the squares to position 2. The baseline shift was effected to simulate cameras attached to a moving aircraft. In each sketch the symbol with the cross represents the location of the central spot in the small (plywood) resection set of figure 10. This gives some feeling for the change in pointing angle for the two cases. The distance to the core was calculated using all conceivable pairs of points which could be triangulated. The histogram in figure 11(b) summarizes 100 measurements of D_c based on these pairings, and the arrow indicates the value determined independently with a steel tape measure.

There is a definite bias (of about 6 in.) of unknown origin in the data. Many of the image points occur in the peripheral field of the frames where the distortions are not fully corrected, and this is a likely source of this error which would be addressed in future implementations. The data do not appear to be bimodal even though they consist of two different baseline orientations. This is encouraging in light of the intended application. The standard deviation of this set is 1.2 ft. Some of this is due to including cases which are weak. For example, pairs involving low-numbered targets occur in the poorly corrected regions of the sensor and appear in the weakest photogrammetric data space since the apparent baseline B appears foreshortened from their perspective, and the line defined by these points is extrapolated greatly to determine D_c.

Conclusions

A novel method for experimentally determining the proximity of a trailing vortex is described. The method is based on standard photogrammetric methods using data from two cameras affixed either to the probe aircraft or to an overflying aircraft. In the latter case the position of the probe aircraft would also be determined by triangulation. Targeting the vortex to permit triangulation points would require *seeding* the vortex with balloons or other targets. Previous work cited in the paper has confirmed that balloons released under certain limited conditions are attracted to and delineate the vortex core under flight conditions. Sunlit balloons can provide adequate high-contrast targets against a clear sky background for image centroiding purposes. This paper has focused on the photogrammetric aspect of the problem and has concluded that there are no obvious "*show stoppers,*" provided a suitable balloon release system is developed which allows balloon entrainment in the vortex cores.

Core ranging using a coordinate frame attached to the moving probe aircraft apparently does not seriously degrade ranging accuracy. The analysis has assumed that cameras could maintain their relative orientations throughout the measurement time frame. The practical implementation would require means for targeting the core with high contrast targets every several hundred feet.

NASA Langley Research Center
Hampton, VA 23665-5225
July 17, 1989

APPENDIX

Development of the Collinearity Equations

The photogrammetric model is based on the collinearity equations which relate ideal (i.e., nonaberrated) photo and object point coordinates based on projection through a perspective center. The relative orientation of the image coordinate frame with respect to the laboratory frame is arbitrary and can be described in many equivalent ways. The unnecessary confusion which can result from these preferences when reading the literature or in deriving analytic expressions for simplified geometries given a particular choice can be avoided if the transformation is decomposed into its elementary operations.

Figure 12 depicts a single perspective center O and photo plane $x'y'$ in the XYZ laboratory system. Actually there exist two perspective centers which correspond, in a perfect system, to the front and rear nodal points of the camera lens. For this discussion O merely specifies the mathematical transformation involved. It is essential to realize that the $x'y'z'$ photo frame and the XYZ laboratory frame are initially parallel to and displaced from one another. A perpendicular line dropped to the photo plane from O penetrates at point (x'_p, y'_p), which is designated as the principal point by photogrammetrists and unfortunately conflicts with well-established usage in optics for characterizing first-order imaging systems. The perpendicular distance is identified as the camera constant c.

The line connecting points P and O intersects the photo plane at $p(x'y')$. A vectorial description helps to define this collineation. The perspective center can be described by $\mathbf{R}_c = \begin{pmatrix} X_c \\ Y_c \\ Z_c \end{pmatrix}$ in the lab frame or $\mathbf{r}'_c = \begin{pmatrix} x'_p \\ y'_p \\ c \end{pmatrix}$ in the photo system. Image coordinate $\mathbf{r}' = \begin{pmatrix} x' \\ y' \\ 0 \end{pmatrix}$ locates p.

Let $\mathbf{R}$ locate point P in space. Then (see fig. 12) unit vector $\hat{u}$ from O to P (or p) can be described in either frame.

$$\hat{u} = \frac{\mathbf{r}' - \mathbf{r}'_c}{|\mathbf{r}' - \mathbf{r}'_c|} = \frac{\mathbf{R} - \mathbf{R}_c}{|\mathbf{R} - \mathbf{R}_c|} \tag{A1}$$

Rearranging,

$$\mathbf{r}' - \mathbf{r}'_c = \frac{|\mathbf{r}' - \mathbf{r}'_c|}{|\mathbf{R} - \mathbf{R}_c|}(\mathbf{R} - \mathbf{R}_c) \equiv \lambda(\mathbf{R} - \mathbf{R}_c) \tag{A2a}$$

where the scale factor λ has been defined by the last equality and in general varies from point to point in the image except for object planes strictly parallel to the image plane. The scale factor corresponds to the linear magnification $\frac{\textit{Image distance}}{\textit{Object distance}}$ in simple optics. An arbitrary camera orientation may be described by consecutive rotational transformations. For example, in the popular $\omega\phi\kappa$ description the coordinates are first rotated through angle ω about x, then rotated by ϕ about the new y', and finally through κ about the reoriented z'-axis. If unprimed coordinates are used to describe the fully rotated photo coordinates then

$$\mathbf{r} = \begin{pmatrix} \cos\kappa & \sin\kappa & 0 \\ -\sin\kappa & \cos\kappa & 0 \\ 0 & 0 & 1 \end{pmatrix} \begin{pmatrix} \cos\phi & 0 & -\sin\phi \\ 0 & 1 & 0 \\ \sin\phi & 0 & \cos\phi \end{pmatrix} \begin{pmatrix} 1 & 0 & 0 \\ 0 & \cos\omega & \sin\omega \\ 0 & -\sin\omega & \cos\omega \end{pmatrix} \begin{pmatrix} x' \\ y' \\ z' \end{pmatrix} \equiv M\mathbf{r}' \tag{A3}$$

where the matrix M has been defined by the last equality. Standard matrix multiplication may be used to identify the following matrix components:

$$\begin{cases} m_{11} = \cos\kappa\cos\phi \\ m_{12} = \sin\kappa\cos\omega + \cos\kappa\sin\phi\sin\omega \\ m_{13} = \sin\kappa\sin\omega - \cos\kappa\sin\phi\cos\omega \\ m_{21} = -\sin\kappa\cos\phi \\ m_{22} = \cos\kappa\cos\omega - \sin\kappa\sin\phi\sin\omega \\ m_{23} = \cos\kappa\sin\omega + \sin\kappa\sin\phi\cos\omega \\ m_{31} = \sin\phi \\ m_{32} = -\cos\phi\sin\omega \\ m_{33} = \cos\phi\cos\omega \end{cases}$$

where angles are positive if counterclockwise when viewing from the positive axis toward the origin. These equations are consistent with equations (2.23) of reference 3 or equations (B-21) of reference 8.

The matrix M operating on equation (A2) removes the primes from the left-hand side and we are left with

$$\begin{pmatrix} x - x_p \\ y - y_p \\ 0 - c \end{pmatrix} = \lambda \begin{pmatrix} m_{11} & m_{12} & m_{13} \\ m_{21} & m_{22} & m_{23} \\ m_{31} & m_{32} & m_{33} \end{pmatrix} \begin{pmatrix} X - X_c \\ Y - Y_c \\ Z - Z_c \end{pmatrix} \tag{A2b}$$

which written in component form becomes

$$\left.\begin{aligned} x - x_p &= \lambda[m_{11}(X - X_c) + m_{12}(Y - Y_c) + m_{13}(Z - Z_c)] \\ y - y_p &= \lambda[m_{21}(X - X_c) + m_{22}(Y - Y_c) + m_{23}(Z - Z_c)] \\ -c &= \lambda[m_{31}(X - X_c) + m_{32}(Y - Y_c) + m_{33}(Z - Z_c)] \end{aligned}\right\} \tag{A4}$$

The third equation may be used to eliminate scale λ, thus recovering the standard form for the collinearity equations. (Compare eqs. (2.234) of ref. 3.)

$$\left.\begin{aligned} x - x_p + \frac{c[m_{11}(X - X_c) + m_{12}(Y - Y_c) + m_{13}(Z - Z_c)]}{[m_{31}(X - X_c) + m_{32}(Y - Y_c) + m_{33}(Z - Z_c)]} &= 0 \\ y - y_p + \frac{c[m_{21}(X - X_c) + m_{22}(Y - Y_c) + m_{23}(Z - Z_c)]}{[m_{31}(X - X_c) + m_{32}(Y - Y_c) + m_{33}(Z - Z_c)]} &= 0 \end{aligned}\right\} \tag{A5}$$

Equations (A5) are the governing equations for photogrammetry and relate measured image coordinates (x, y) to points (XYZ) in space. Novices in photogrammetry are often bewildered by sign conventions and apparent handedness changes. As derived, c is a physical length and is therefore always positive. The sign preceding the fraction is correct whenever the image and scene are in correspondence as viewed by an observer from the perspective center. (See fig. 12.) This is the case with video data. When dealing with various hard-copy options, always orient the image to correspond to the scene. Then, if the readup device imposes a requirement (e.g., emulsion side up) which requires say 180° rotation about the y-axis, simply reverse the sign of x. Any number of elementary reorientations can be tracked with this procedure.

For the parallel axis case depicted in figure 3 ($x_p = y_p = 0$), M is the unit matrix, $\mathbf{R}_c' = \begin{pmatrix} -B/2 \\ 0 \\ 0 \end{pmatrix}$, and $\mathbf{R}_c'' = \begin{pmatrix} B/2 \\ 0 \\ 0 \end{pmatrix}$. Then

$$x' - \frac{|c|(X + B/2)}{Z} = 0$$

and

$$x'' - \frac{|c|(X - B/2)}{Z} = 0$$

in agreement with equations (1) and (2).

The following test case is provided to verify program coding for the general case. If

$$\begin{pmatrix} x_p \\ y_p \\ c \end{pmatrix} \equiv \begin{pmatrix} 0.1 \\ 0.1 \\ 12.5 \end{pmatrix}, \begin{pmatrix} \omega \\ \phi \\ \kappa \end{pmatrix} \equiv \begin{pmatrix} 85 \\ -20 \\ -1 \end{pmatrix}, \text{ and } \begin{pmatrix} X_c \\ Y_c \\ Z_c \end{pmatrix} \equiv \begin{pmatrix} -12 \\ -20 \\ 1 \end{pmatrix}$$

then point

$$\begin{pmatrix} X \\ Y \\ Z \end{pmatrix} \equiv \begin{pmatrix} 17 \\ 45 \\ 6 \end{pmatrix} \text{ images to } \begin{pmatrix} x \\ y \end{pmatrix} = \begin{pmatrix} 1.00020212 \\ 2.00745220 \end{pmatrix}$$

and the rotation matrix is

$$M = \begin{pmatrix} +0.93954950 & -0.34218784 & +0.01241848 \\ +0.01639990 & +0.08119611 & +0.99656321 \\ -0.34202014 & -0.93611681 & +0.08189961 \end{pmatrix}$$

References

1. Dunham, R. Earl, Jr.; Verstynen, Harry A., Jr.; and Benner, Margaret S.: Progress Report on Wing-Trailing-Vortex Studies. *NASA Aircraft Safety and Operating Problems, Volume I,* NASA SP-270, 1971, pp. 101–113.
2. Verstynen, Harry A., Jr.; and Dunham, R. Earl, Jr.: *A Flight Investigation of the Trailing Vortices Generated by a Jumbo Jet Transport.* NASA TN D-7172, 1973.
3. Slama, Chester C., ed.: *Manual of Photogrammetry,* Fourth ed. American Soc. of Photogrammetry, c.1980.
4. Burner, A. W.; Snow, W. L.; and Goad, W. K.: Close-Range Photogrammetry With Video Cameras. *Technical Papers—51st Annual Meeting ASP, Volume 1,* American Soc. of Photogrammetry, c.1985, pp. 62–77.
5. Burner, A. W.; Snow, W. L.; Goad, W. K.; and Childers, B. A.: A Digital Video Model Deformation System. *ICIASF '87,* IEEE Catalog No. 87CH2449-7, Inst. of Electrical and Electronics Engineers, Inc., c.1987, pp. 210–220.
6. Brown, Duane C.: *Application of Close-Range Photogrammetry to Measurements of Structures in Orbit, Volume 2. (Appendices).* GSI Tech. Rep. No. 80-012 (Contract No. MOM7DNS-895942), Geodetic Services Inc., Sept. 15, 1980.
7. Hasinger, Siegfried H.: An Experiment With Particles in a Free Vortex. *AIAA J.,* vol. 6, no. 5, May 1968, pp. 939–940.
8. Wolf, Paul R.: *Elements of Photogrammetry.* McGraw-Hill, Inc., c.1974.

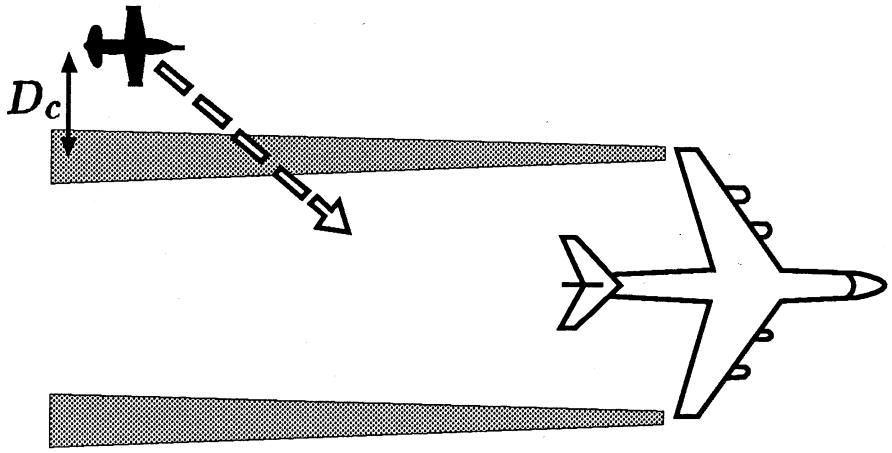

Figure 1. Sketch indicating desired measurement variable; D_c is the perpendicular distance from the instrumented aircraft to the vortex core.

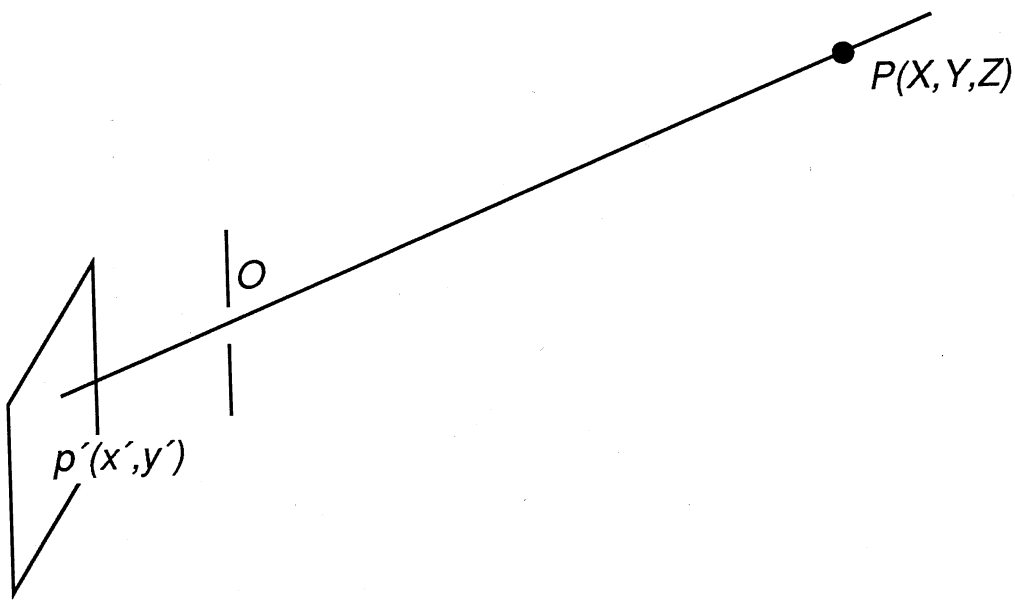

Figure 2. Sketch depicting the collinearity transformation. A point P in three-dimensional space is projected onto a two-dimensional detector surface through perspective center O.

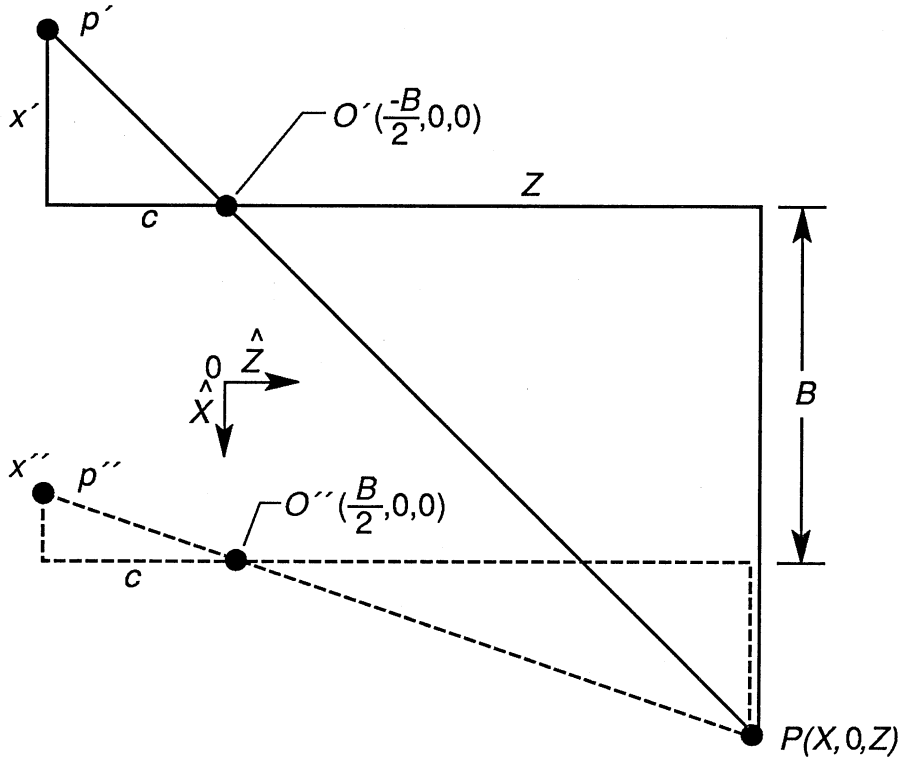

Figure 3. Geometry for triangulation using parallel axis cameras. Cameras are separated by baseline B. Figure 3 is used to derive equations (1), (2), and (3).

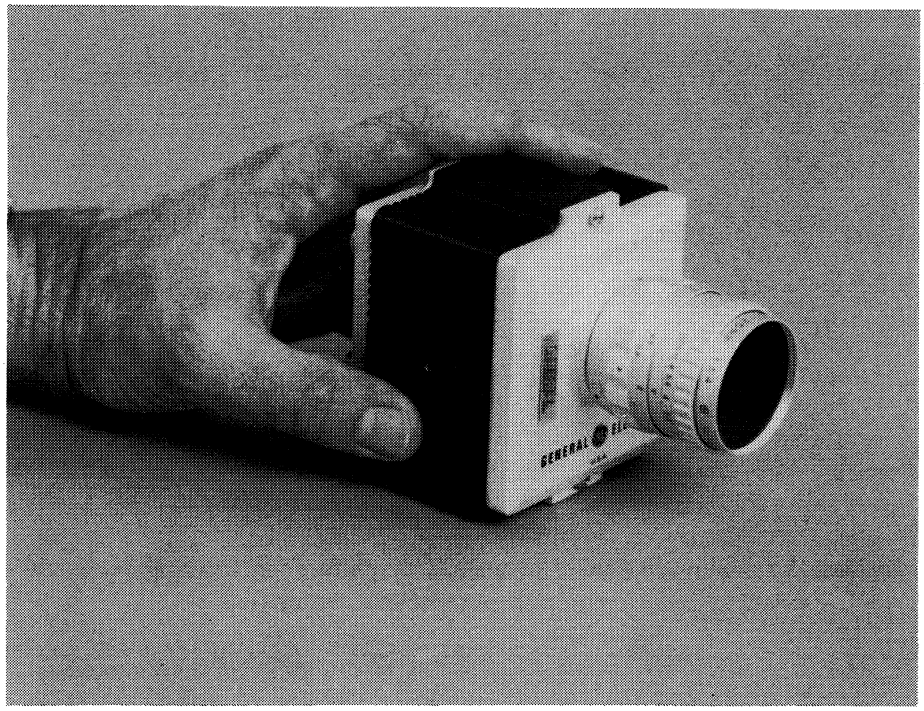

Figure 4. Example of current solid-state image camera.

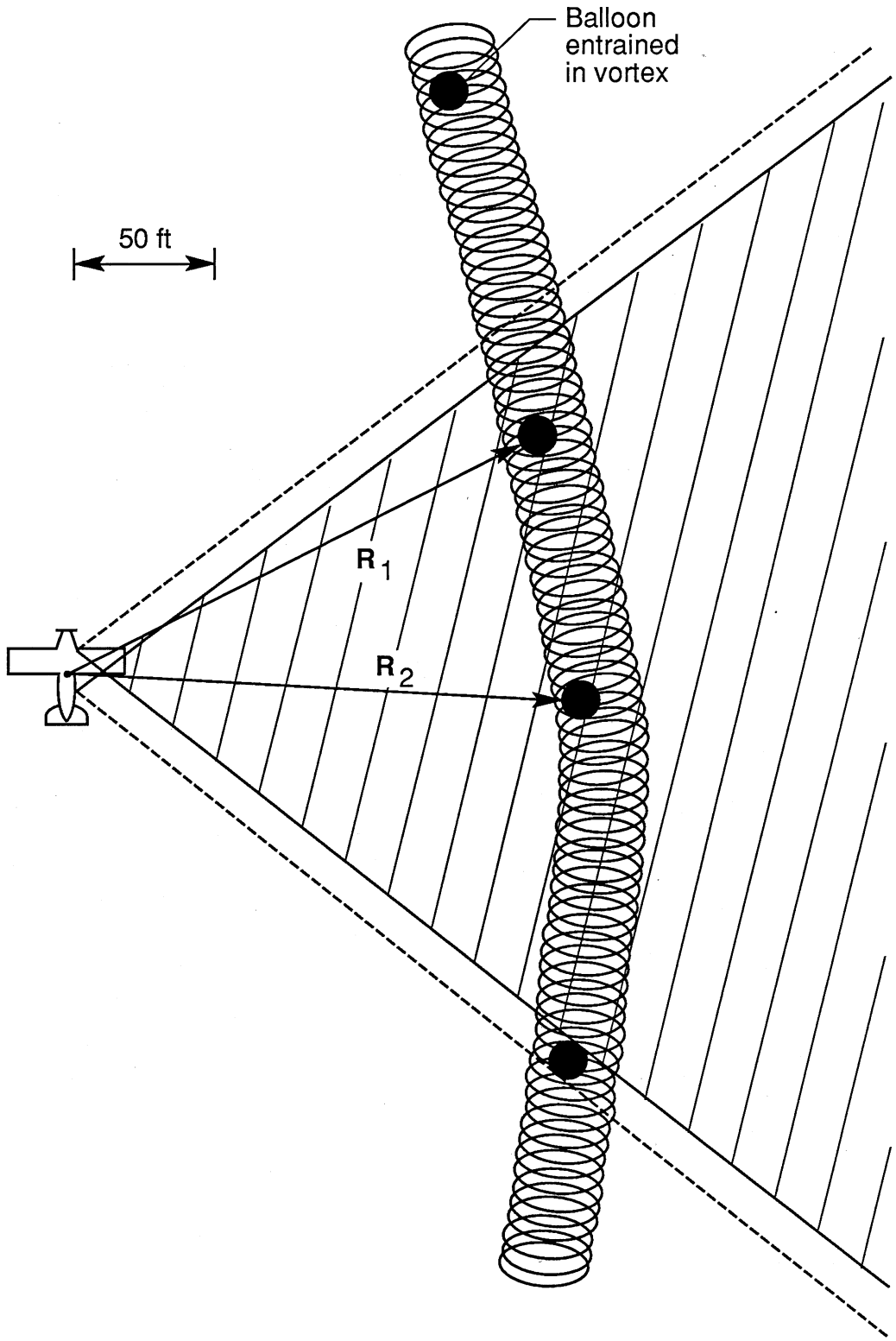

Figure 5. Eagle's-eye view of the probe aircraft approaching the targeted vortex core. Cameras placed fore and aft mutually cover the hatched area, allowing triangulation ranging of targets.

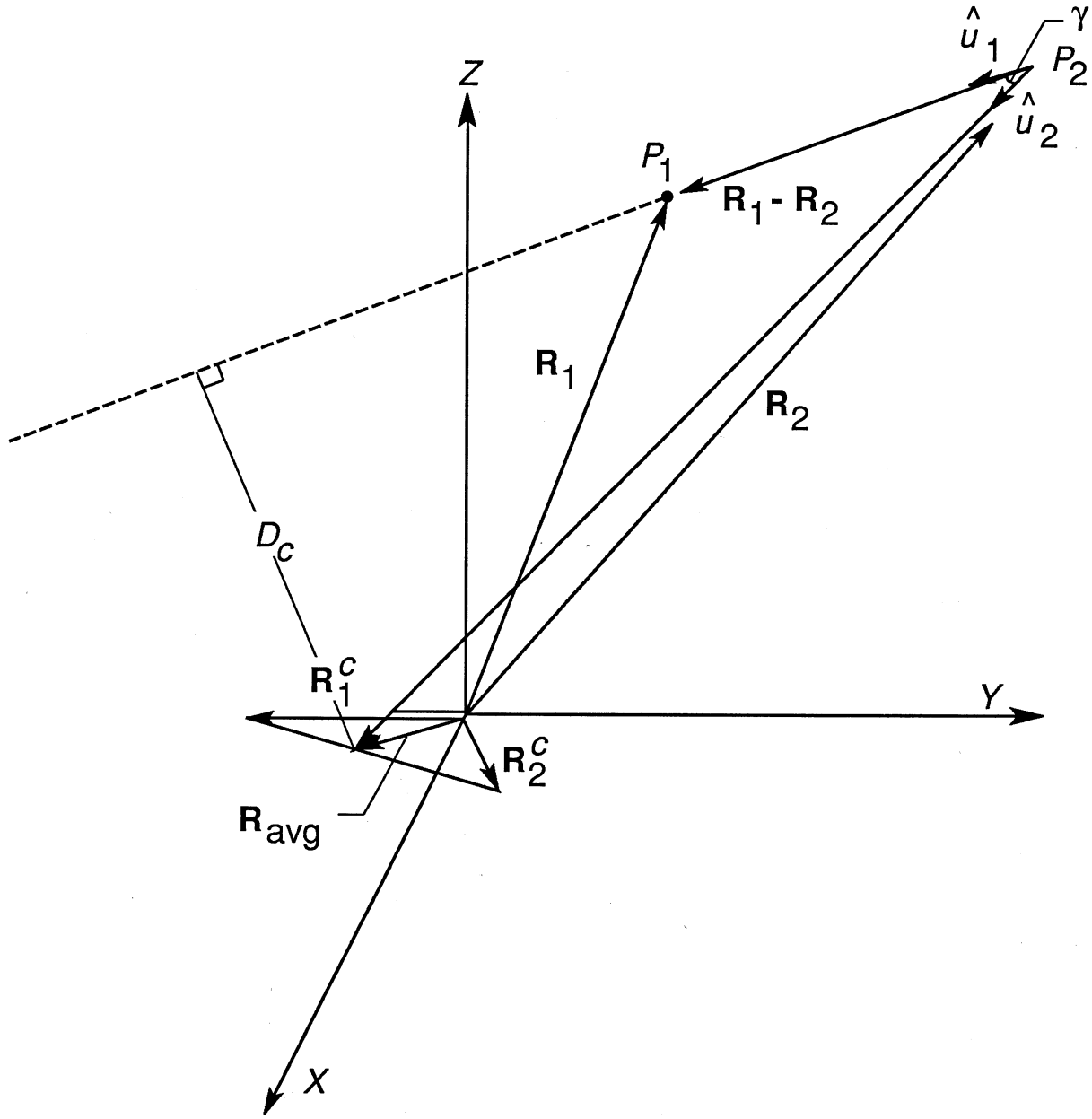

Figure 6. Geometry used to derive equation (4). Points P_1 and P_2 are on the vortex core. Perspective centers for the cameras are located at $\mathbf{R}_1^c$ and $\mathbf{R}_2^c$ on the aircraft in the proximity of the trailing vortex.

Mylar balloon, shiny surface

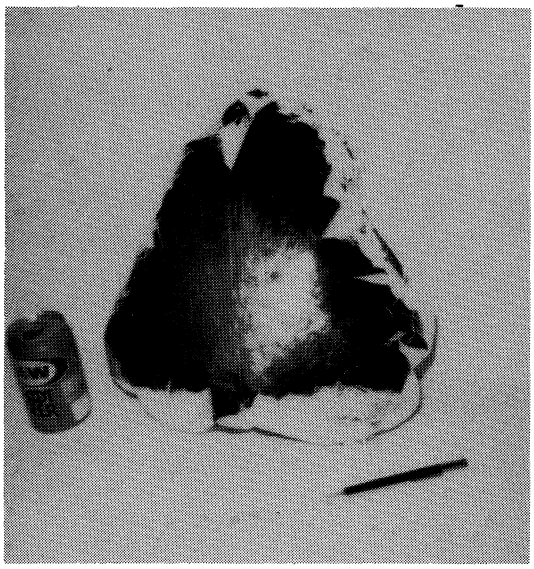

Mylar balloon, buff surface

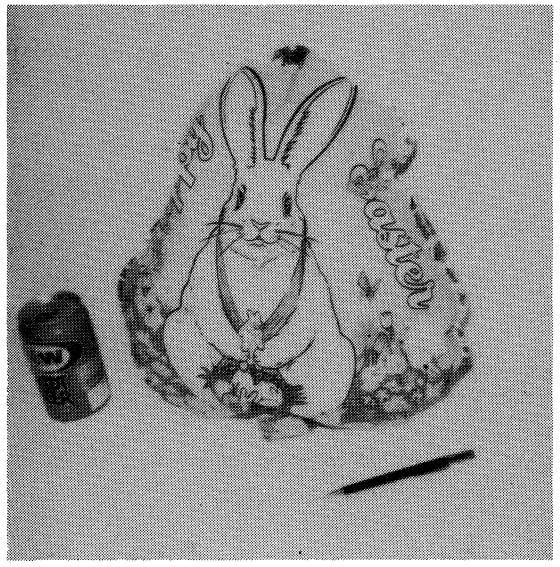

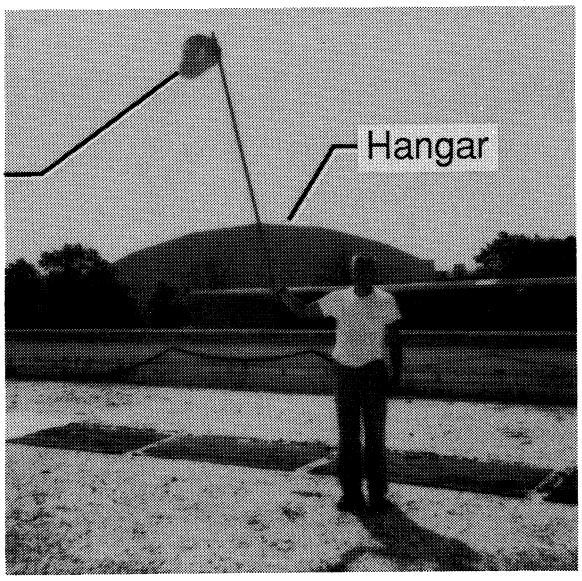

Figure 7. Pictures of a metalized party balloon used to experiment with detectability. The balloon was tethered to a stick as shown in the lower photo and held on the hangar roof in the background. A series of pictures was acquired from the same position used to take the lower snapshot.

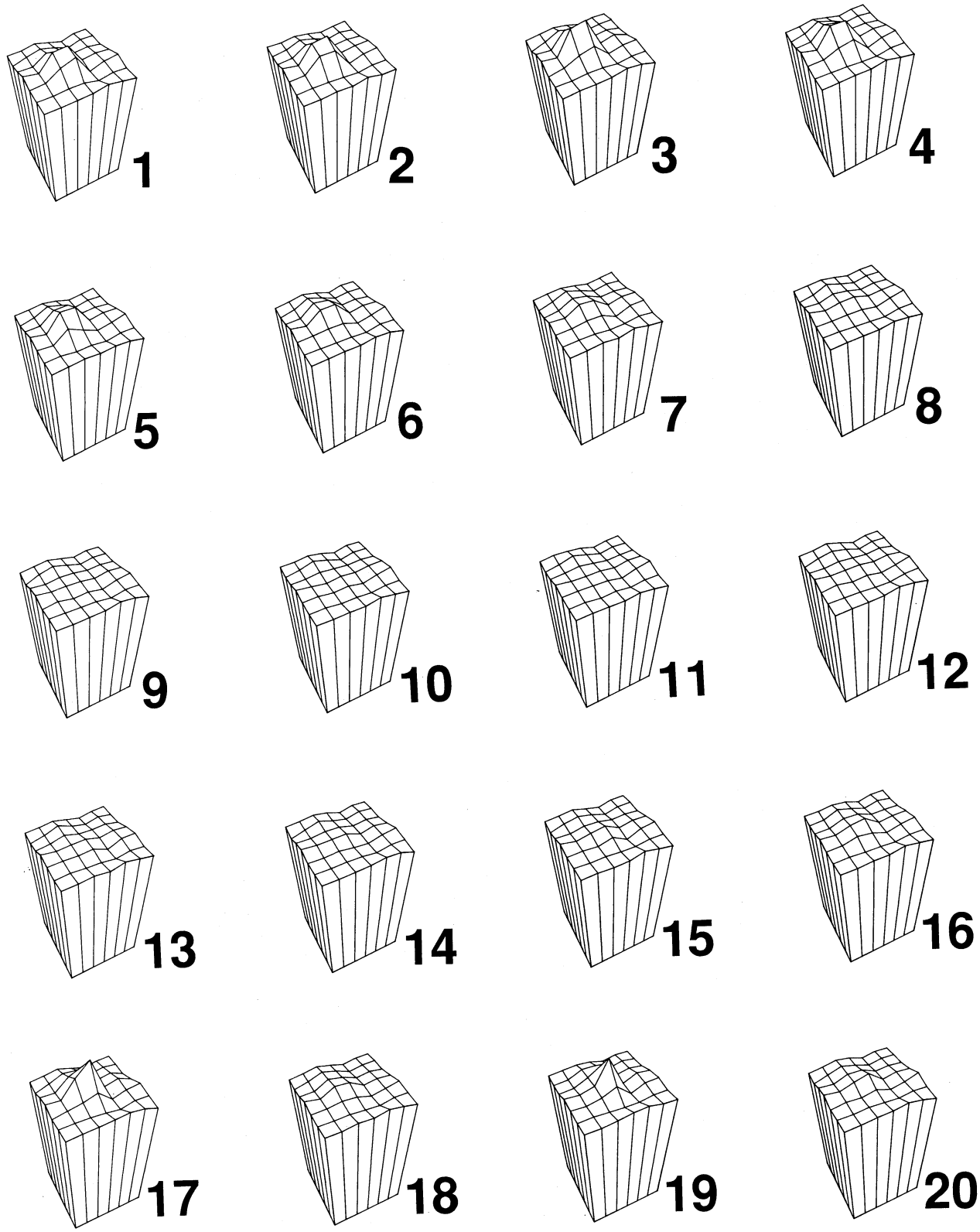

Figure 8. Intensity plots in the vicinity of the balloon shown in the previous photo. Relative intensity is displayed in the vertical direction. Frames were taken at 50 msec intervals.

(a) Ground-launched balloons before the overflight of the vortex-generating aircraft.

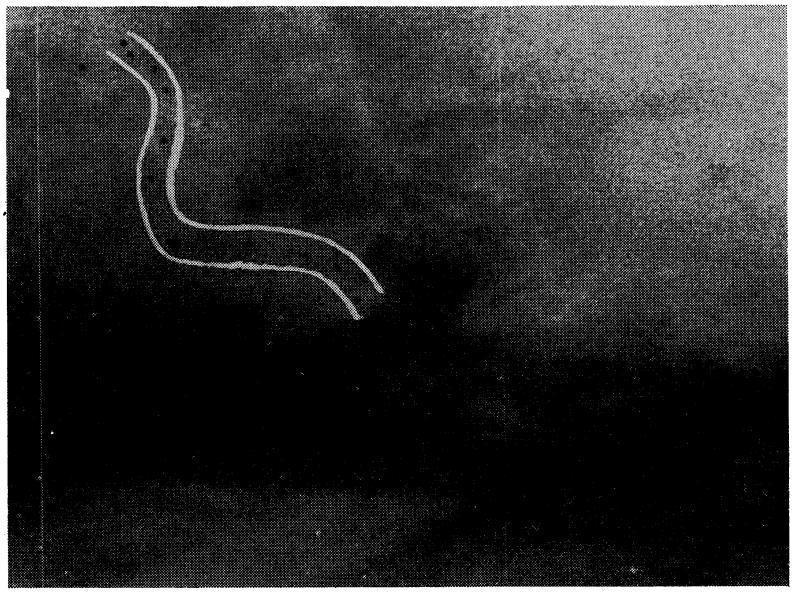

(b) Partial ordering of the balloons as they become captured by the vortex after the light aircraft flew over.

L-89-35

Figure 9. Enlargements of two frames from 16-mm film used to study entrainment of balloons in trailing wingtip vortices.

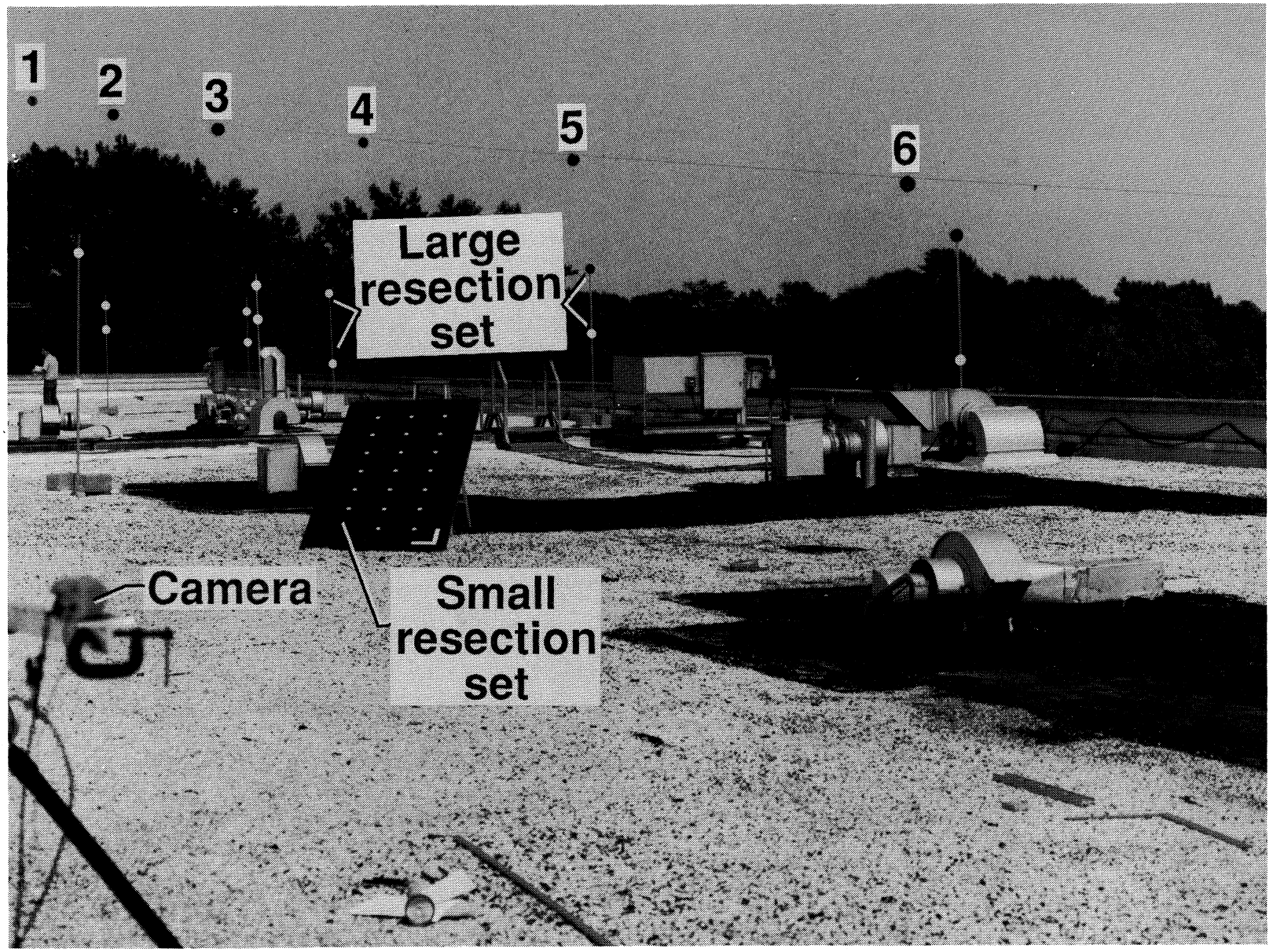

Figure 10. Experimental arrangement used to mock up a vortex core geometry.

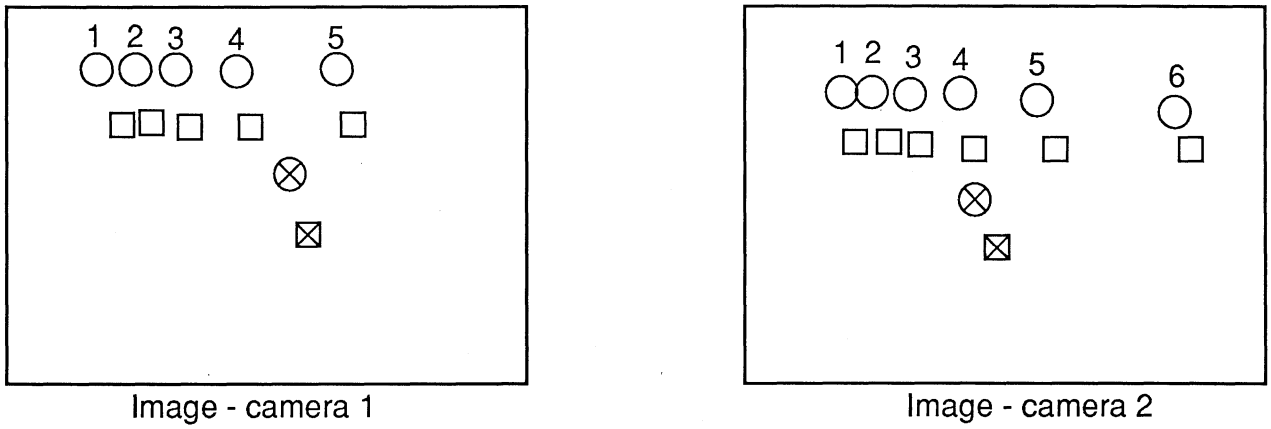

(a) Image coordinate locations of targets in figure 10. Data for two baseline orientations (circles and squares) are overlaid.

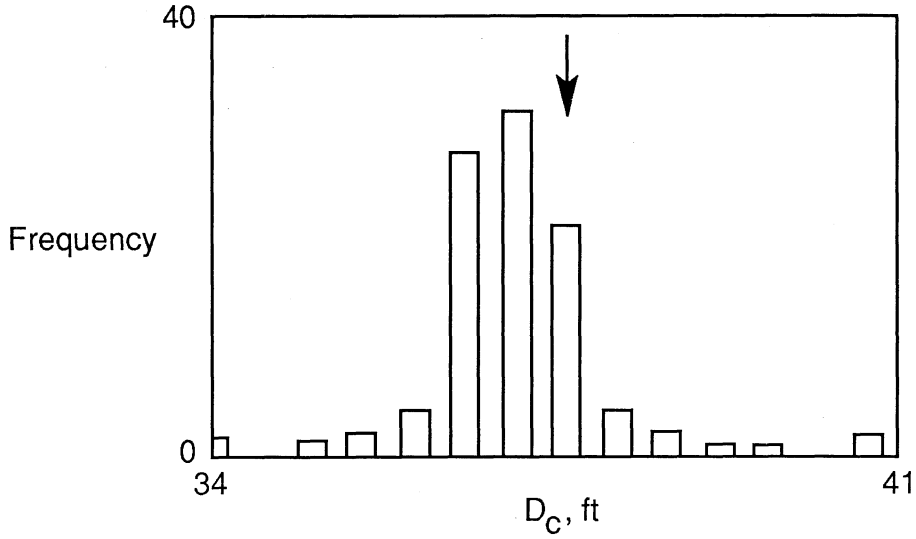

(b) Histogram representing 100 determinations of D_c based on target pairs.

Figure 11. Results from one data sequence.

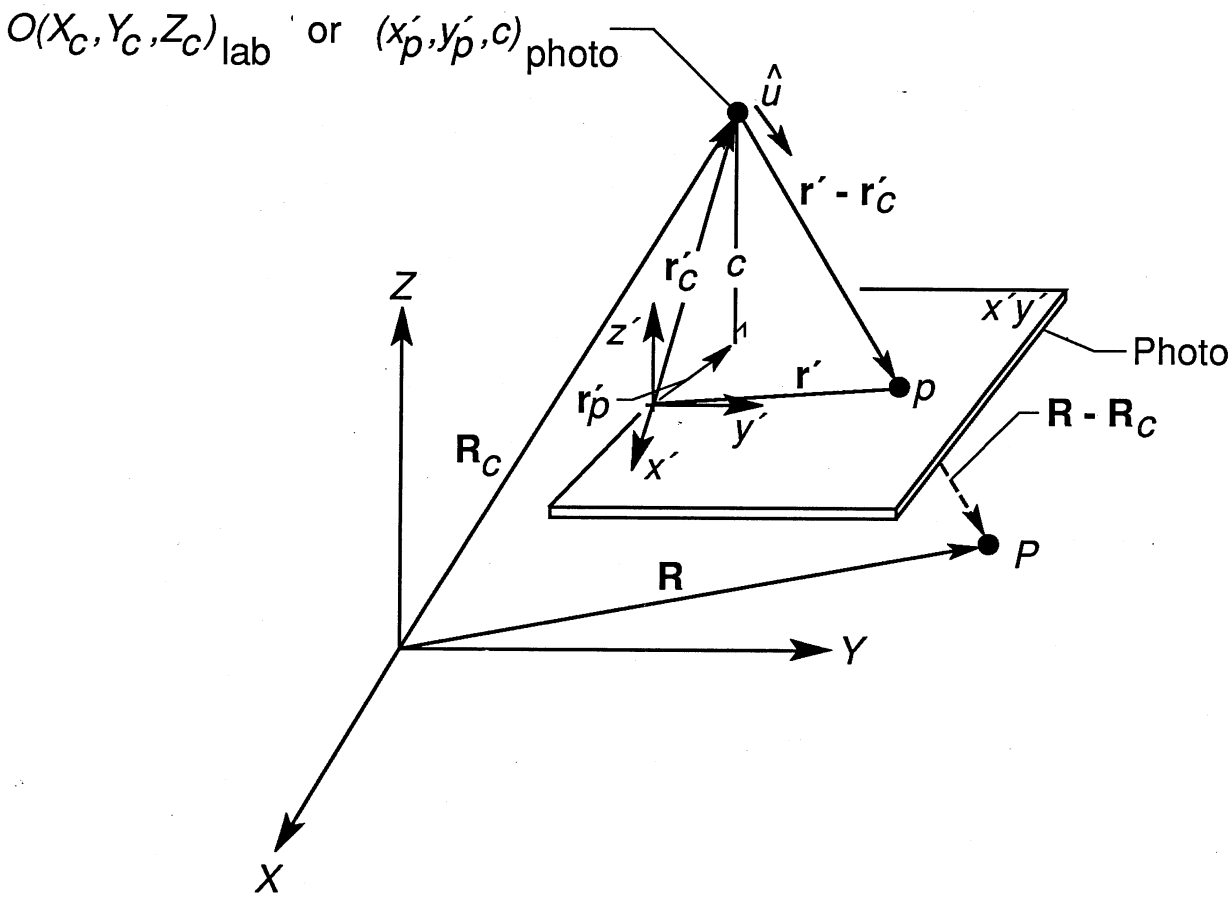

Figure 12. Relationship of pertinent variables in the collinearity transformation.

NASA
National Aeronautics and Space Administration

Report Documentation Page

1. Report No. NASA TM-4129	2. Government Accession No.	3. Recipient's Catalog No.
4. Title and Subtitle Photogrammetric Technique Using Entrained Balloons for In-Flight Ranging of Trailing Vortices		5. Report Date October 1989
		6. Performing Organization Code
7. Author(s) Walter L. Snow, Alpheus W. Burner, and William K. Goad		8. Performing Organization Report No. L-16551
9. Performing Organization Name and Address NASA Langley Research Center Hampton, VA 23665-5225		10. Work Unit No. 505-61-01-05
		11. Contract or Grant No.
12. Sponsoring Agency Name and Address National Aeronautics and Space Administration Washington, DC 20546-0001		13. Type of Report and Period Covered Technical Memorandum
		14. Sponsoring Agency Code

15. Supplementary Notes

16. Abstract

A novel method for experimentally determining the radial distance of a probe aircraft from a trailing vortex is described. The method relies on photogrammetric triangulation of targets entrained in the vortex core. The report describes the theory and preliminary testing using laboratory mock-ups. Solid-state video cameras would be used to provide data at 30-Hz rates. Practical methods for seeding the vortex are under separate investigation and are not treated in this report. The report concludes that the methodology is sound.

17. Key Words (Suggested by Authors(s)) Photogrammetry, Balloons, Trailing vortices, CCD camera, Aircraft wakes	18. Distribution Statement Unclassified–Unlimited Subject Category 35

19. Security Classif. (of this report) Unclassified	20. Security Classif. (of this page) Unclassified	21. No. of Pages 21	22. Price A03

For sale by the National Technical Information Service, Springfield, Virginia 22161-2171